

X-ray topography characterization of gallium nitride substrates for power device development

Balaji Raghothamachar^{a,*}, Yafei Liu^a, Hongyu Peng^a, Tuerxun Ailihumaer^a, Michael Dudley^a, F. Shadi Shahedipour-Sandvik^b, Kenneth A. Jones^c, Andrew Armstrong^d, Andrew A. Allerman^d, Jung Han^e, Houqiang Fu^f, Kai Fu^f, Yuji Zhao^f

^a Department of Materials Science & Chemical Engineering, Stony Brook University, Stony Brook, NY 11794, USA

^b 257 Fuller Road, SUNY Polytechnic Institute, Albany, NY 12203, USA

^c Army Research Laboratory, RDRL-SED-E, Adelphi, MD 20783, USA

^d Sandia National Laboratory, Albuquerque, NM 87185, USA

^e Department of Electrical Engineering, Yale University, New Haven, CT 06511, USA

^f School of Electrical, Computer, and Energy Engineering, Arizona State University, Tempe, AZ 85287, USA

ARTICLE INFO

Communicated by M.S. Goorsky

Keywords:

A1. Characterization
A1. Defects
A1. X-ray topography
A1. Substrates
A3. Hydride vapor phase epitaxy
B1. Nitrides

ABSTRACT

Gallium nitride substrates grown by the hydride vapor phase epitaxy (HVPE) method using a patterned growth process have been characterized by synchrotron monochromatic beam X-ray topography in the grazing incidence geometry. Images reveal a starkly heterogeneous distribution of dislocations with areas as large as 0.3 mm^2 containing threading dislocation densities below 10^3 cm^{-2} in between a grid of strain centers with higher threading dislocation densities ($> 10^4 \text{ cm}^{-2}$). Basal plane dislocation densities in these areas are as low as 10^4 cm^{-2} . By comparing the recorded images of dislocations with ray tracing simulations of expected dislocations in GaN, the Burgers vectors of the dislocations have been determined. The distribution of threading screw/mixed dislocations (TSDs/TMDs), threading edge dislocations (TEDs) and basal plane dislocations (BPDs) is discussed with implications for fabrication of power devices.

1. Introduction

The wide bandgap semiconductor, gallium nitride (GaN), has applications in optoelectronic devices such as light emitting diodes and laser diodes, as well as in power electronic devices such as switches and inverters. GaN along with the other wide bandgap semiconductors, especially silicon carbide (SiC), are being developed to replace silicon in power electronic devices because of their large electric breakdown field, higher current density and thermal conductivity, faster switching and lower on-resistance. Realization of GaN power devices requires affordable, high quality GaN wafers for commercialization. However, the development of bulk GaN of high structural quality is limited by the available growth techniques for GaN. Melt growth techniques are precluded for GaN and therefore other growth techniques have to be employed including crystallization from gas phase, solution and their combinations. The high pressure, high temperature method yields high

quality, but small crystals [1]. Physical vapor transport (PVT) method [2,3] development has been very limited, and the Na-flux method [4,5] has yet to be successfully commercialized. The ammonothermal growth method [6,7] is capable of producing high quality crystals and sizes up to 2" in diameter are commercially available, but in limited quantities. This technique is limited by low growth rates and potentially high point defect concentrations. Currently, hydride vapor phase epitaxy (HVPE) [8,9] i.e. crystallization from the gas phase at ambient pressure is the most common approach for manufacturing GaN substrates at high growth rates ($> 100 \mu\text{m/hr}$) and high purity. However, these substrates are grown on foreign substrates, such as sapphire, gallium arsenide or silicon carbide and suffer from large dislocation densities ($> 10^6 \text{ cm}^{-2}$) due to significant differences in lattice parameters and coefficients of thermal expansion. These lead to high densities of defects such as threading dislocations and grain boundaries, as well as considerable bowing of crystallographic planes, all of which contribute to lowered

* Corresponding author.

E-mail addresses: balaji.raghothamachar@stonybrook.edu (B. Raghothamachar), Yafei.liu@stonybrook.edu (Y. Liu), hongyu.peng@stonybrook.edu (H. Peng), tuerxun.ailihumaer@stonybrook.edu (T. Ailihumaer), Michael.dudley@stonybrook.edu (M. Dudley), sshahedipour-sandvik@sunypoly.edu (F.S. Shahedipour-Sandvik), Kenneth.a.jones162.civ@mail.mil (K.A. Jones), aarmstr@sandia.gov (A. Armstrong), aaaller@sandia.gov (A.A. Allerman), jung.han@yale.edu (J. Han), houqiang@asu.edu (H. Fu), kaifu@asu.edu (K. Fu), yuji.zhao@asu.edu (Y. Zhao).

<https://doi.org/10.1016/j.jcrysgr.2020.125709>

Received 15 December 2019; Received in revised form 4 May 2020; Accepted 5 May 2020

Available online 19 May 2020

0022-0248/ © 2020 Elsevier B.V. All rights reserved.

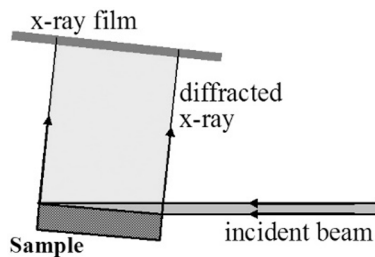


Fig. 1. Schematic of the grazing incidence geometry using the synchrotron monochromatic X-ray beam.

yield and degraded device performance.

To overcome the limitations of using foreign substrates for HVPE growth, patterned growth methods [9] have been developed to lower the dislocation densities. These patterned growth methods can concentrate dislocations to small areas leaving the remaining regions relatively dislocation-free ($<10^2 \text{ cm}^{-2}$). These methods were initially developed and successfully implemented for fabricating violet laser diodes [10]. Such substrates can potentially also be employed for fabricating GaN-based power devices. However, for power device applications, the presence of certain types of dislocations can be deleterious. It has been shown that threading dislocations, especially those with a screw component, play an important role in reverse-bias current leakage in GaN diodes [11,12]. In 2016, a more recent study by Horibuchi, et al. showed that under heat treatment, helical dislocations can form above threading dislocations, which can have a significant impact on the performance of the devices fabricated in the area [13]. On the other hand, the role of basal plane dislocations during device operation while studied in considerable detail in silicon carbide power devices [14–16] has not been investigated in GaN-based power devices. Therefore, in order for these substrates to be used for power devices, a detailed knowledge of the microstructure (i.e. the type and distribution of dislocations) is necessary. In this study, a detailed characterization of this distribution has been carried out non-destructively using synchrotron X-ray topography in conjunction with ray tracing simulations to determine the distribution of various types of dislocations present in a typical HVPE GaN substrate growth by the patterned method.

2. Experiment

HVPE GaN substrates (single side polished) obtained from Mitsubishi Chemical Corporation [9] and grown by the patterned

method similar to that described in [10], were imaged by synchrotron X-ray topography [17] at beamline 1-BM, Advanced Photon Source at Argonne National Laboratory. The defects of interest are primarily the threading dislocations that terminate at the surface of the substrate that will replicate into the overgrown epilayer, as well as basal plane dislocations (BPDs) close to the surface that can potentially propagate into the epilayer. To image these defects, the grazing incidence geometry (Fig. 1) is particularly suitable. In grazing-incidence reflection, a very small incident angle is used (typically 2°) and the $1\ 1\ \bar{2}\ 4$ reflection is recorded (39.13° to $(0\ 0\ 0\ 1)$ surface). The penetration depth of the x-ray beams, t_p^k in the grazing incidence geometry for defective crystals is determined by photoelectric absorption and given by:

$$t_p^k = \frac{1}{\mu \left(\frac{1}{\sin\Phi_0 + \sin\Phi_H} \right)} \quad (1)$$

where μ is the absorption coefficient (cm^{-1}) of GaN at the X-ray energy used, Φ_0 is the incident angle ($\sim 2^\circ$) and Φ_H ($\sim 80.13^\circ$) is the exit angle with the surface of the sample. For the $1\ 1\ \bar{2}\ 4$ reflection for GaN at 9.37 keV, the penetration depth based on photoelectric absorption is calculated to be approximately $2\ \mu\text{m}$. While the X-ray beam is large enough to cover the entire sample at the grazing angle, lattice distortions (strains, tilts, curvature) limit the actual region diffracted at a set angle. In order to image the entire area, the sample is rotated about an axis parallel to the $[1\ \bar{1}\ 0\ 0]$ direction in steps of 0.015° to obtain an effective misorientation contour map.

For comparison purposes, HVPE GaN substrates produced by growth on non-patterned foreign substrates have also been imaged. The images were recorded on high resolution Agfa Structurix D3sc X-ray films.

3. Ray tracing simulations

A ray-tracing simulation based on an orientation contrast mechanism provides an excellent tool to qualitatively and quantitatively interpret the dislocation images on X-ray topographs. It has been successfully used in back-reflection X-ray topography to clarify the screw character of the micropipes in SiC [18]. It also has been used to reveal the dislocation sense of screw dislocations [19], the Burgers vectors of threading edge dislocations [20], the core structure of Shockley partial dislocations [21] and the sign of Frank partial dislocations [22]. Ray tracing simulations have also similarly been used to characterize threading screw and edge dislocations in AlN [23] and ZnO [24]. Sintonen, et al. simulated images of threading screw and mixed dislocations in back reflection X-ray topography in GaN and correlated those with defects images from GaN grown by the ammonothermal method

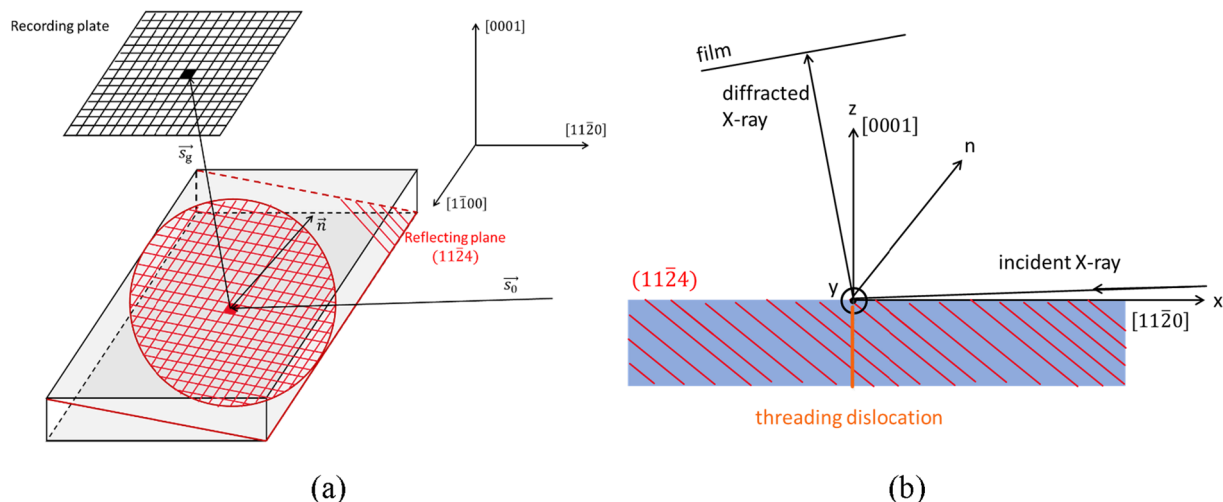


Fig. 2. (a) Schematic diagram for ray-tracing simulation; (b) Coordinate system setup used for ray tracing simulation in grazing incidence geometry.

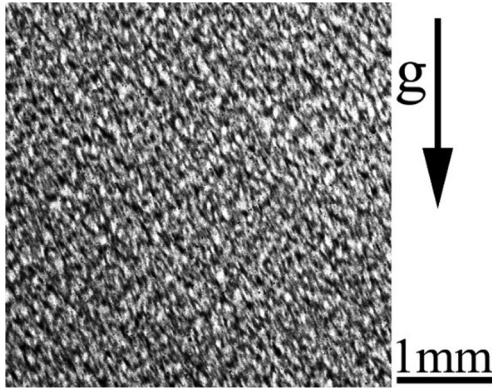


Fig. 3. Reflection topograph from the Ga face of a HVPE GaN wafer showing a uniform, but high, density of dislocations ($>10^6/\text{cm}^2$).

[25]. The back reflection geometry is insensitive to sense of dislocations and threading edge and basal plane dislocations are out of contrast on these images. The use of grazing incidence geometry overcomes these limitations and can be used to characterize all dislocations present.

In ray-tracing simulations the mosaic region around the dislocation (or other defect) is divided into a large number of cubic diffraction units with their local misorientations coinciding with the long-range displacement field of the dislocation or defect. The key point is to obtain the plane normal after distortion due to the strain fields associated with the defects. The plane normal $\bar{n}(x, y, z)$ after distortion is given by

$$\bar{n}(x, y, z) = \bar{n}^0(x, y, z) - \nabla[\bar{n}^0(x, y, z) \cdot \bar{u}(x, y, z)] \quad (2)$$

where $\bar{n}^0(x, y, z)$ is the plane normal before distortion and $\bar{u}(x, y, z)$ is the displacement field of the dislocation or other defect. When X-rays are incident (with incidence wave vector \mathbf{s}_0) on the crystal surface, local distortion on the reflecting planes will result in the variation of diffracted beam directions \mathbf{s}_g . The diffracted beam direction is given by $\mathbf{s}_0 \times \mathbf{n} = -\mathbf{n} \times \mathbf{s}_g$. Diffracted beams with slightly different directions will be collected on the recording plane, and contrast is formed as the diffracted beams are overlapped or separated. A schematic of the ray-tracing simulation principle is shown in Fig. 2(a) and the coordinate system employed for the simulation is illustrated in Fig. 2(b).

In the case of a pure screw type dislocation, the displacement field, \mathbf{u} , is purely along the z axis and is given by [26]:

$$u_z = \frac{b}{2\pi} \arctan\left(\frac{y}{x}\right) \quad (3)$$

where b is the Burgers vector of c, i.e. [0 0 0 1].

An additional displacement in the c-plane caused by the surface relaxation effect should also be taken into consideration. This effect takes place when the threading dislocation is close to the free surface of the crystal because the strain components perpendicular to the surface have to be zero in order to satisfy the free surface boundary conditions. These are given by [26]:

$$u_x = u_\theta \frac{-y}{\sqrt{x^2 + y^2}} \quad (4)$$

$$u_y = u_\theta \frac{x}{\sqrt{x^2 + y^2}} \quad (5)$$

where

$$u_\theta = -\frac{b}{2\pi} \sum_{n=0}^{\infty} (-1)^n \left\{ \frac{\sqrt{x^2 + y^2}}{(2n+1)t - z + \sqrt{[(2n+1)t - z]^2 + (x^2 + y^2)}} - \frac{\sqrt{x^2 + y^2}}{(2n+1)t + z + \sqrt{[(2n+1)t + z]^2 + (x^2 + y^2)}} \right\}.$$

For pure edge type dislocation, a new coordinate system should be

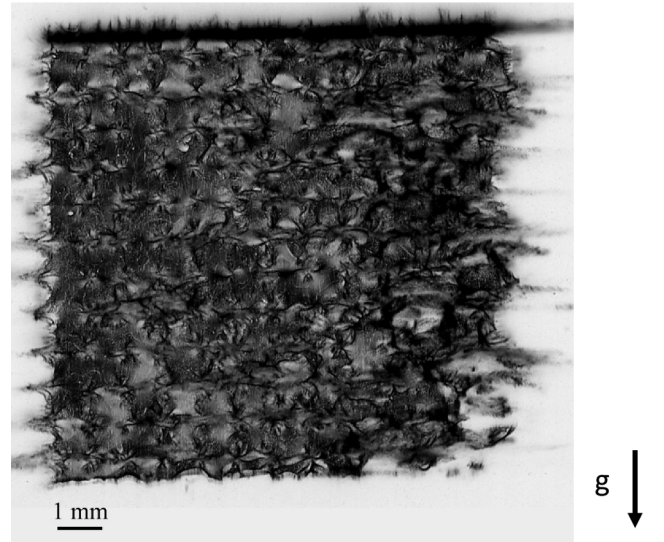


Fig. 4. Synchrotron monochromatic beam grazing incidence X-ray topograph ($\mathbf{g} = 1 \ 1 \ 2 \ 4$; 9.37 KeV) showing the microstructure of a HVPE GaN substrate wafer. A mesh of strain centers is observed with a heterogeneous distribution of threading and basal dislocations emanating from most centers.

set where the x-axis is parallel to the Burgers vector's direction. The displacement field is given by [27]:

$$u_x = \frac{b}{2\pi} \left[\tan^{-1} \frac{y}{x} + \frac{xy}{2(1-\nu)(x^2 + y^2)} \right] \quad (6)$$

$$u_y = -\frac{b}{2\pi} \left[\frac{1-2\nu}{4(1-\nu)} \ln(x^2 + y^2) + \frac{x^2 - y^2}{4(1-\nu)(x^2 + y^2)} \right] \quad (7)$$

where ν is the Poisson's ratio. The displacements as written approximate the wurtzite-structure GaN as isotropically elastic materials.

Wolfram Mathematica® 12 is used to carry out the simulation process. In the code, a coordinate system is initially selected. Then, the wave vector of the incident beam and plane normal of a perfect lattice are calculated so that the position of the dislocation image on the film is located. After that, a matrix is set up to store the intensity map of the diffracted beam. Finally, an intensity map of the stored matrix is plotted.

4. Results and discussion

4.1. Experimental results

A reflection topograph from a typical unpatterned HVPE GaN wafer (Note: Wafer not provided by Mitsubishi Chemical Corporation) is shown in Fig. 3. The topograph shows a defective crystalline layer free from inhomogeneous strains and characterized by a more or less uniform distribution of defects. However, no individual defects are resolved from which the defect density is estimated to be greater than $10^6/\text{cm}^2$, the limit of resolution for x-ray topography. A comparison of the X-ray images with the corresponding optical photograph (not shown here) reveals some elongation or contraction of the X-ray image. This distortion is due to bending of lattice planes from residual stresses. These stresses originate from the thermal expansion coefficient mismatch of GaN with the foreign substrate (sapphire, GaAs or SiC) on which the GaN was grown.

A grazing incidence topograph recorded from a 10 mm \times 10 mm patterned HVPE GaN wafer is shown in Fig. 4. The image reveals a

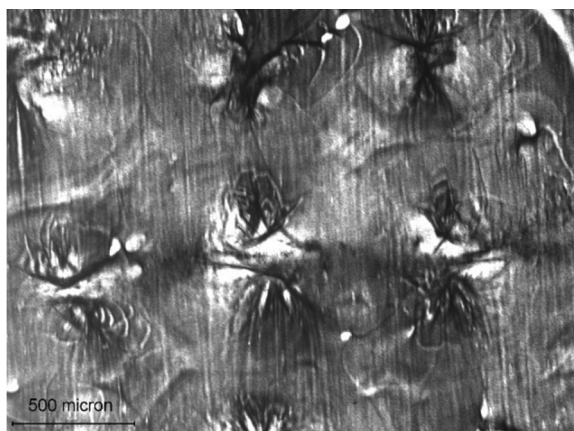


Fig. 5. High magnification X-ray grazing incidence topograph showing the defect distribution around a single strain center. Note the inhomogeneous distortion at the strain center and threading dislocations scattered near it. BPDs emanating from the strain center propagate deep into the surrounding regions.

microstructure characterized by a periodic pattern that originates from the patterned growth process employed to lower the dislocation density and stress in the substrate. The pattern consists of a grid or mesh (spacing $\sim 800 \mu\text{m}$) of strain centers (*i.e.* regions of high distortion

caused by inhomogeneous strains and tilts) that originate at the patterned array of exposed regions where the film originally nucleated on the dissimilar substrate. Based on the mechanism of defect reduction employed for this patterned growth process, these regions contain a high density of dislocations, which is not readily resolved on the X-ray topographs. However, the much larger regions between these centers of distortions are characterized as of very low dislocation densities as shown in the high magnification image in Fig. 5 because most threading dislocations remain concentrated near the strain center. However, BPDs emanating from the strain centers sometimes propagate deep into the surrounding regions. Under the high temperatures ($> 1000 \text{ }^\circ\text{C}$) used for subsequent MOCVD growths, implantation annealing and other treatments for device fabrication, these BPDs can potentially glide and multiply under the influence of thermal stresses that are generated. They could then propagate into the previously dislocation-free regions and possibly replicate into the epilayer. The presence of these BPDs could be highly damaging to device operation and likely leading to failure. Therefore, it is critical to limit their spread, especially into the active device regions. The presence of BPDs could, therefore, limit the amount of useful area available for device fabrication, and thusly reduce yield.

Polarized optical microscopy of the surface of the patterned GaN wafer also shows contrast from the patterned growth as shown in Fig. 6(a) and (c). We observe that some centers of strains show bundles of BPDs originating from it and propagating deep into the adjacent regions (Fig. 6(d)).

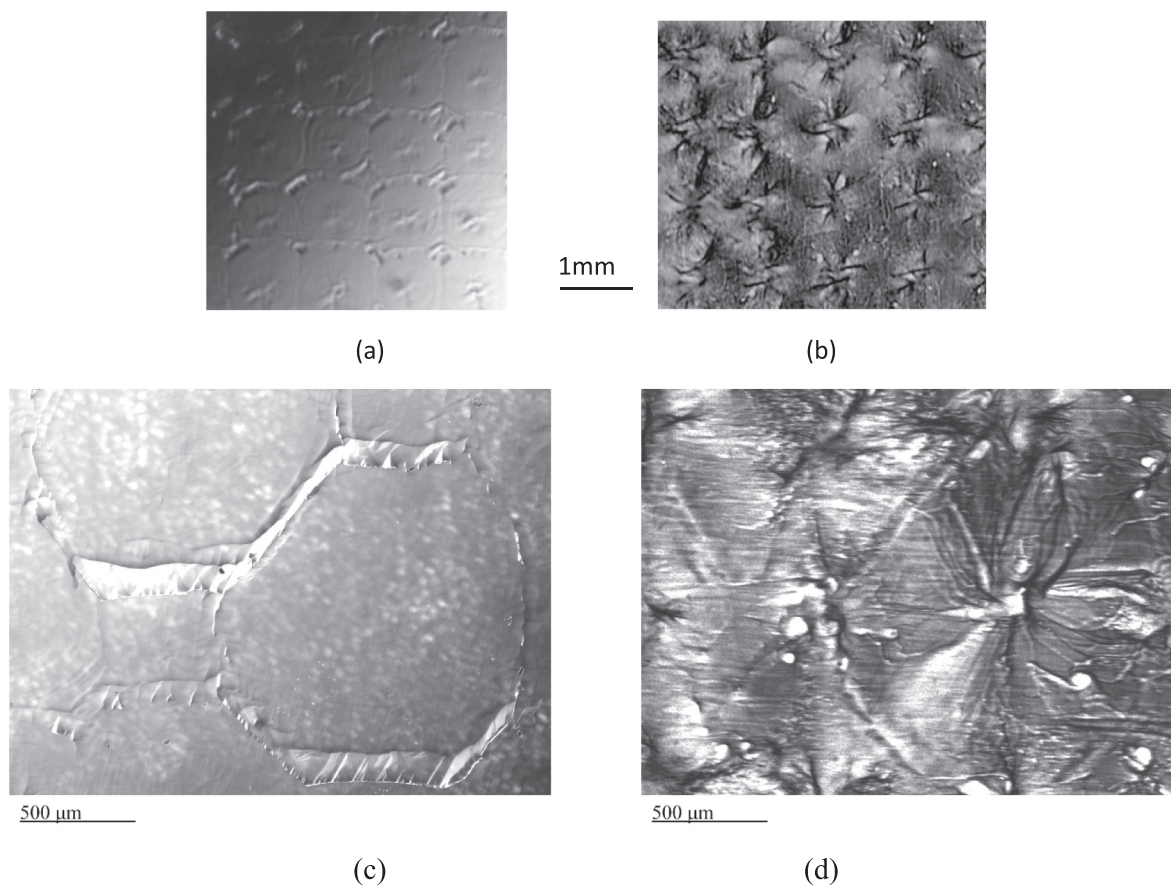


Fig. 6. Polarized optical micrographs (a, c) and corresponding grazing incidence X-ray topographs (b, d) from selected regions of the patterned HVPE GaN substrate wafer. Optical micrographs show contrast from the patterns while X-ray topograph show the dislocation distribution. Note the bundles of dislocations originating from strain centers in (d).

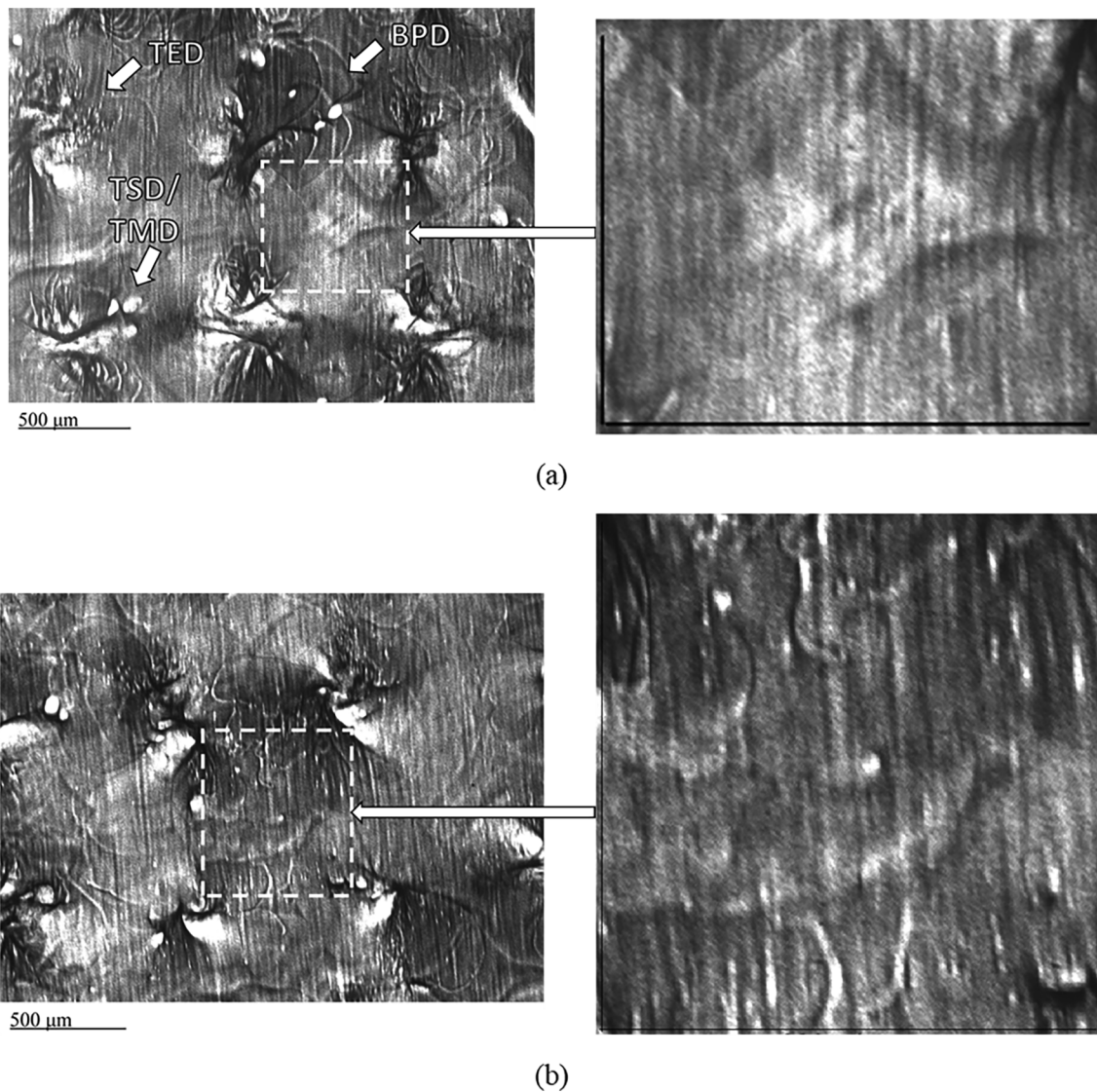


Fig. 7. (a), (b) High magnification X-ray topographs of selected regions of a patterned HVPE GaN wafer showing a distribution of BPDs, TSDs/TMDs and TEDs. Enlarged images inset show the low dislocation density regions where device fabrication can potentially be carried out.

Dislocation density measurements were carried out around selected centers of strain. The dislocation types observed are BPDs, TEDs and TSDs/TMDs. Clearly the regions closer to the strain centers are characterized by high dislocation densities and strains, while further away, few dislocations are observed. A low dislocation density area can be obtained as a $490 \mu\text{m}$ by $610 \mu\text{m}$ rectangle is shown in the inset in Fig. 7(a), where the BPD density is calculated as $9.2 \times 10^4/\text{cm}^2$, while no obvious TSDs and TEDs are observed. However, in another region with a relatively higher dislocation density shown in Fig. 7(b), the area is a rectangle of $642 \mu\text{m}$ by $626 \mu\text{m}$. The BPD density is measured as $1.35 \times 10^5/\text{cm}^2$, and the TSD and TED density are $9.95 \times 10^2/\text{cm}^2$ and $9.85 \times 10^3/\text{cm}^2$ respectively.

4.2. Correlation of X-ray topographs with ray tracing simulations

Using the simulated images of threading dislocations, the Burgers vectors of the dislocations observed on the X-ray topographs have been characterized. This method of characterization eliminates the need to record multiple reflections for conventional Burgers vector analysis and has been extensively applied in SiC, AlN and ZnO crystals as described in earlier sections.

4.2.1. Basal Plane Dislocations (BPDs)

Two types of BPDs are simulated, which are pure edge type and pure screw type. For each type, both of the opposite sign Burgers vectors are adopted. As seen in Fig. 8(b), for edge type BPD the contrast appears to be either bright or dark, while screw type BPDs show bright and dark contrasts at the same time. On Fig. 8(a), the topograph shows curved BPD segments. The contrast varies from white to black/white. Few dark contrast BPDs are observed.

4.2.2. Threading Screw Dislocations (TSDs)

Single TSDs with Burgers vectors of $+c$ and $-c$ are simulated and correlated with X-ray topography images, as shown in Fig. 9, to characterize their Burgers vectors.

Often opposite sign TSD pairs (Fig. 10(a)) are observed in topography images of the GaN wafer. Comparison with simulated images of opposite pairs of TSDs separated by different distances allows us to determine the separation between these dislocations. For Fig. 11(a), the separation between them is estimated to be around $10 \mu\text{m}$.

4.2.3. Threading Edge Dislocations (TEDs)

According to the extra atomic half planes associated with the TEDs,

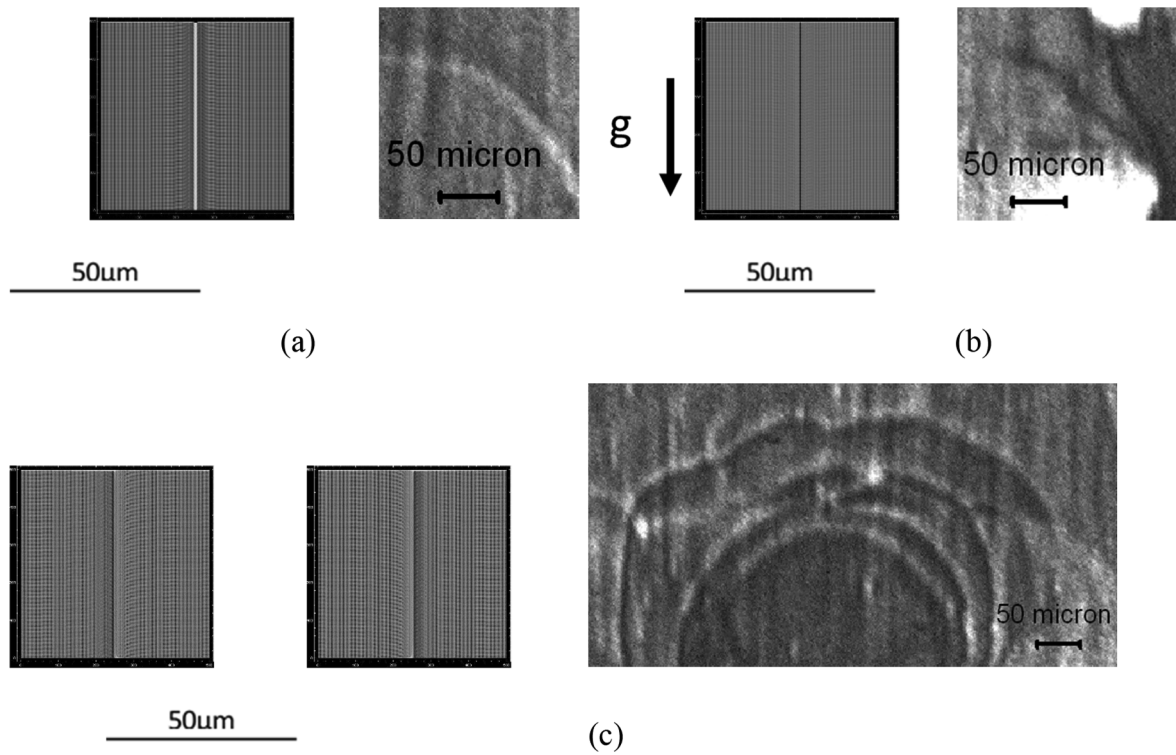


Fig. 8. Ray tracing simulated images of different types of straight BPDs in GaN (at left in each panel) and corresponding X-ray topography images from patterned a HVPE GaN wafer showing curved BPDs (at right each panel). (a) Edge type (+); (b) Edge type (-); (c) Screw type (right and left handed).

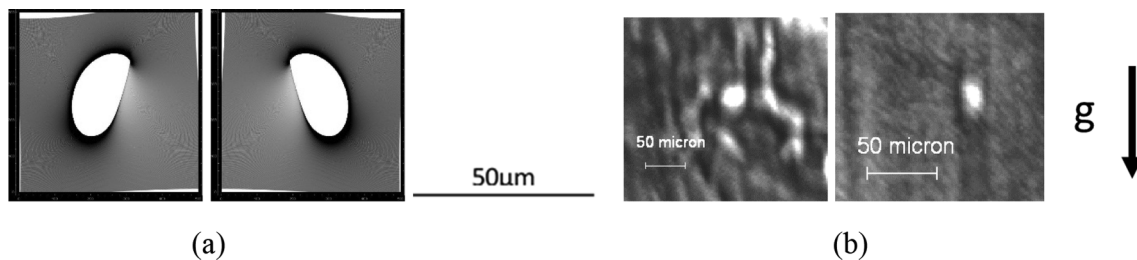


Fig. 9. (a) Ray tracing simulated images of TSDs with Burgers vectors of +c (left) and -c (right) in GaN; (b) Corresponding X-ray topography images from wafer.

six different types of TEDs are simulated (Fig. 11(a)). Their Burgers vectors are at 60° , 120° , 180° , 240° , 300° and 0° counterclockwise to the g-vector on the X-ray films, which in this case is $[1 \ 1 \ \bar{2} \ 0]$.

4.2.4. Threading Mixed Dislocations (TMDs)

TMDs have both c and a components, and therefore there are 12 combinations between opposite sign c-components and 6 different types of a-components. It is noted that the tilt direction of the ellipse in the contrast is to the right when the c-component of the Burgers vector is positive while it is tilted to the left when the c-component of the Burgers vector is negative (Fig. 12).

5. Conclusions

Synchrotron X-ray topography in conjunction with ray tracing simulations has been successfully used to characterize the type and distribution of dislocations in patterned HVPE GaN substrate wafers. Areas as large as 0.3 mm^2 with threading dislocation densities below 10^2

cm^{-2} are observed in between a grid of strain centers with relatively higher threading dislocation densities ($>10^4 \text{ cm}^{-2}$). Basal plane dislocation densities in these areas are as low as 10^4 cm^{-2} . The Burgers vectors of some of these dislocations have been determined by comparison with ray tracing simulations. The areas of low dislocation densities are comparable to the 0.23 mm^2 active device area for 1.2 kV GaN vertical power FinFETs [28] and are thus potentially suitable for fabrication of vertical power devices, but larger areas will be needed for higher voltage devices.

CRediT authorship contribution statement

Balaji Raghothamachar: Data curation, Writing - original draft. **Yafei Liu:** Investigation, Data curation, Writing - original draft. **Hongyu Peng:** Investigation. **Tuerxun Ailihumaer:** Investigation. **Michael Dudley:** Conceptualization, Supervision. **F. Shadi Shahedipour-Sandvik:** Supervision. **Kenneth A. Jones:** Supervision. **Andrew Armstrong:** . **Andrew A. Allerman:** . **Jung Han:** Supervision.

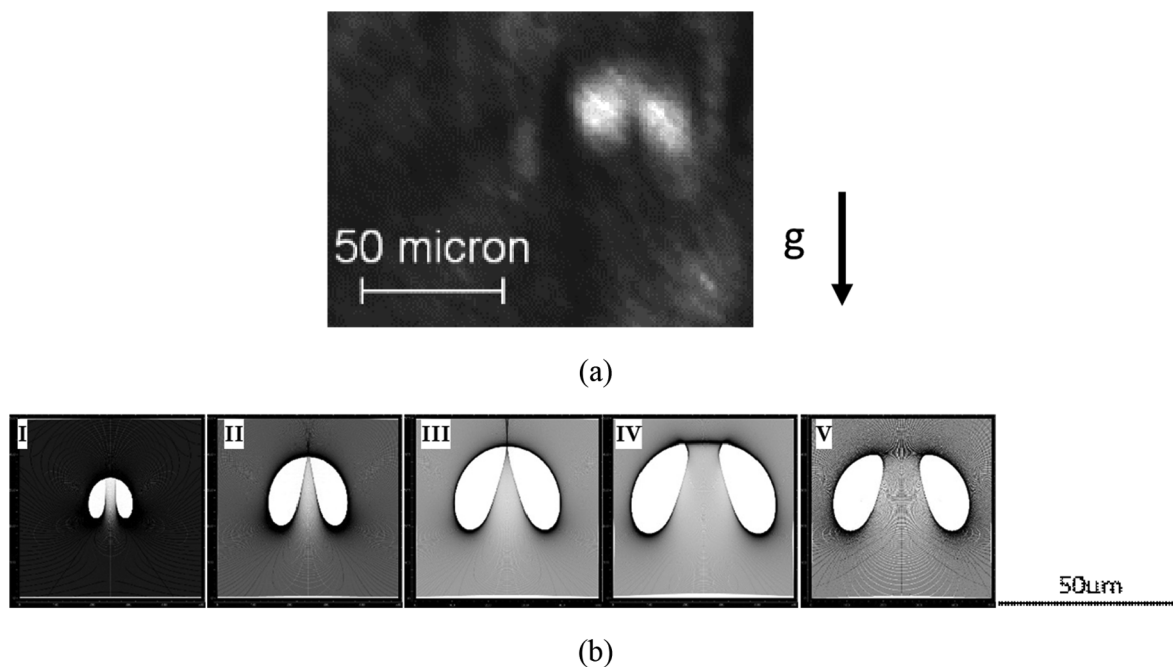


Fig. 10. (a) X-ray topograph showing contrast from opposite sign pairs of TSDs; (b) Ray tracing simulated images of opposite sign TSD pairs with distances of 1 μm , 5 μm , 10 μm , 20 μm , and 40 μm (from left to right). Comparison with the X-ray topograph indicates a separation of around 10 μm (I) between the dislocations.

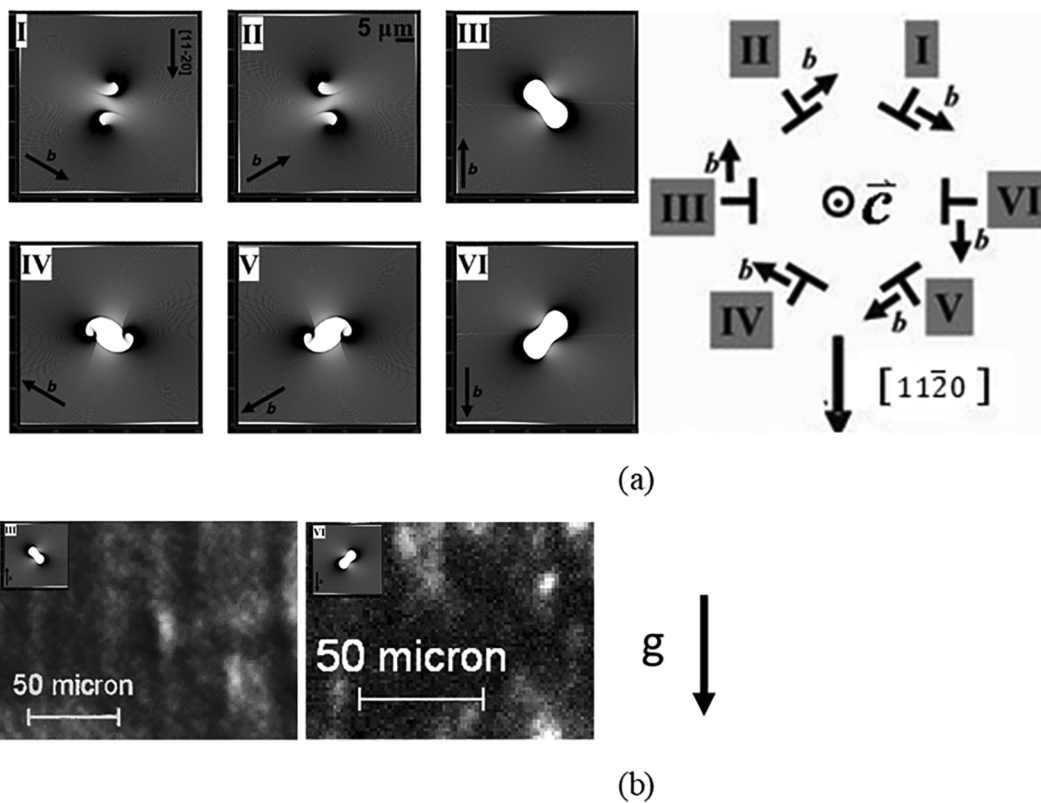


Fig. 11. (a) Simulated images of the 6 different types of TEDs that can be present in GaN. The Burgers vectors are $\frac{1}{3}[1\ 2\ \bar{1}\ 0]$, $\frac{1}{3}[\bar{2}\ 1\ 1\ 0]$, $\frac{1}{3}[1\ 1\ 2\ 0]$, $\frac{1}{3}[1\ \bar{2}\ 1\ 0]$, $\frac{1}{3}[2\ \bar{1}\ \bar{1}\ 0]$ and $\frac{1}{3}[1\ 1\ \bar{2}\ 0]$, respectively (b) Images of TEDs on X-ray topographs with inset simulated images corresponding to their likely Burgers vectors.

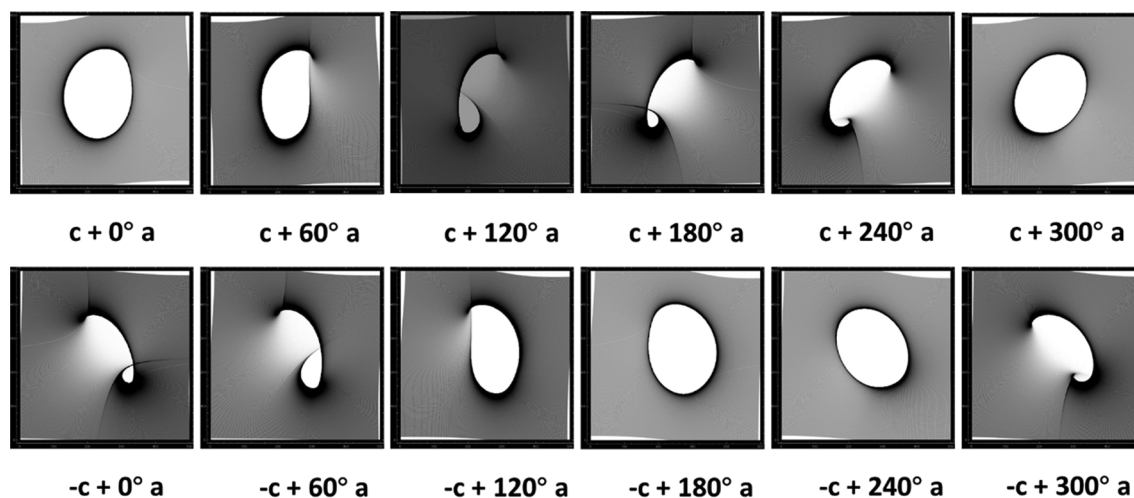


Fig. 12. Simulated images of 12 different types of $c + a$ type threading mixed dislocations. The Burgers vectors calculated is listed in Table 1.

Table 1
Burgers vectors of TMDs simulated in Fig. 12.

	$c + 0^\circ a$	$c + 60^\circ a$	$c + 120^\circ a$	$c + 180^\circ a$	$c + 240^\circ a$	$c + 300^\circ a$
Burgers Vector	$\frac{1}{3}[1 \ 1 \ \bar{2} \ 3]$	$\frac{1}{3}[\bar{1} \ 2 \ \bar{1} \ 3]$	$\frac{1}{3}[2 \ 1 \ 1 \ 3]$	$\frac{1}{3}[\bar{1} \ \bar{1} \ 2 \ 3]$	$\frac{1}{3}[1 \ \bar{2} \ 1 \ 3]$	$\frac{1}{3}[2 \ \bar{1} \ \bar{1} \ 3]$
	$-c + 0^\circ a$	$-c + 60^\circ a$	$-c + 120^\circ a$	$-c + 180^\circ a$	$-c + 240^\circ a$	$-c + 300^\circ a$
Burgers Vector	$\frac{1}{3}[1 \ 1 \ \bar{2} \ \bar{3}]$	$\frac{1}{3}[\bar{1} \ 2 \ \bar{1} \ \bar{3}]$	$\frac{1}{3}[2 \ 1 \ 1 \ \bar{3}]$	$\frac{1}{3}[\bar{1} \ \bar{1} \ 2 \ \bar{3}]$	$\frac{1}{3}[1 \ \bar{2} \ 1 \ \bar{3}]$	$\frac{1}{3}[2 \ \bar{1} \ \bar{1} \ \bar{3}]$

Houqiang Fu: Investigation. Kai Fu: Investigation. Yuji Zhao: Supervision, Writing - review & editing.

Declaration of Competing Interest

The authors declare that they have no known competing financial interests or personal relationships that could have appeared to influence the work reported in this paper.

Acknowledgements

X-ray topography work supported by ARPA-E through PNDIODES program (Project Director: I. Kizilyalli). Synchrotron x-ray topographs were recorded using the resources of the Advanced Photon Source (Beamline 1-BM), a U.S. DOE Office of Science User Facility operated for the DOE Office of Science by Argonne National Laboratory under contract no. DE-AC02-06CH11357. Joint Photon Sciences Institute at Stony Brook University provided partial support for travel and subsistence at the Advanced Photon Source. The authors acknowledge Stephen R. Lee from Sandia National Laboratory for useful discussion and comments. Sandia National Laboratories is a multi-mission laboratory managed and operated by National Technology and Engineering Solutions of Sandia, LLC, a wholly owned subsidiary of Honeywell International, Inc., for the U.S. Department of Energy's National Nuclear Security Administration under contract DE-NA-0003525. The views expressed in the article do not necessarily represent the views of the U.S. Department of Energy or the United States Government.

References

- [1] S. Porowski, I. Grzegory, *J. Cryst. Growth* 178 (1997) 174.
- [2] H. Wu, J. Spinelli, P. Konkapaka, M.G. Spencer, Materials Research Society Symposium Proceedings, 892 (GaN, AlN, InN and Related Materials), 757–762, 2006.
- [3] D. Siche, D. Gogova, S. Lehmann, T. Fizia, R. Fornari, M. Andrasch, A. Pipa, *J. Ehlbeck, J. Cryst. Growth* 318 (2011) 406.
- [4] M. Aoki, H. Yamane, M. Shimada, S. Sarayma, F.J. DiSalvo, *J. Cryst. Growth* 242 (2002) 70.
- [5] Y. Mori, M. Imade, M. Maruyama, M. Yoshimura, *ECS J. Sol. State Sci. Tech.* 2 (2013) N3068.
- [6] R. Dwilinski, R. Doradzinski, J. Garczynski, L.P. Sierzputowski, A. Puchalski, Y. Kanbara, K. Yagi, H. Minakuchi, H. Hayashi, *J. Cryst. Growth* 310 (2008) 3911.
- [7] T. Hashimoto, F. Wu, J.S. Speck, S. Nakamura, *J. Cryst. Growth* 310 (2008) 3907.
- [8] H.P. Maruska, J.J. Tietjen, *Appl. Phys. Lett.* 15 (1969) 327.
- [9] T. Nakamura, K. Motoki, *Proc. IEEE* 101 (2013) 2221.
- [10] K. Fujito, S. Kubo, H. Nagaoka, T. Mochizuki, H. Namita, S. Nagao, *J. Cryst. Growth* 311 (2009) 3011.
- [11] J.W.P. Hsu, M.J. Manfra, D.V. Lang, S. Richter, S.N.G. Chu, A.M. Sergent, R.N. Kleiman, L.N. Pfeiffer, R.J. Molnar, *Appl. Phys. Lett.* 78 (2001) 1685.
- [12] E.J. Miller, E.T. Yu, P. Waltereit, J.S. Speck, *Appl. Phys. Lett.* 84 (2004) 535.
- [13] K. Horibuchi, S. Yamaguchi, Y. Kimoto, K. Nishikawa, T. Kachi, *Semicond. Sci. Technol.* 31 (2016) 034002.
- [14] M. Skowronski, S. Ha, *J. Appl. Phys.* 99 (2006) 011101.
- [15] Y. Chen, M. Dudley, K.X. Liu, R.E. Stahlbush, *Appl. Phys. Lett.* 90 (2007) 171930.
- [16] K. Maeda, Radiation-enhanced dislocation glide: the current status of research, in: O. Ueda, S. Pearton (Eds.), *Materials and Reliability Handbook for Semiconductor Optical and Electron Devices*, Springer, New York, NY, 2013.
- [17] B. Raghathamachar, G. Dhanaraj, M. Dudley in *Handbook of Crystal Growth*, G. Dhanaraj, K. Byrappa, V. Prasad, M. Dudley, Springer, 2010, p. 1425.
- [18] X.R. Huang, M. Dudley, W.M. Vetter, W. Huang, S. Wang, C.H. Carter Jr., *Appl. Phys. Lett.* 74 (1999) 353.
- [19] Y. Chen, M. Dudley, *Appl. Phys. Lett.* 91 (2007) 141918.
- [20] I. Kamata, M. Nagano, H. Tsuchida, Y. Chen, M. Dudley, *Mater. Sci. Forum* 600–603 (2009) 305.
- [21] Y. Chen, M. Dudley, K.X. Liu, J.D. Caldwell, R.E. Stahlbush, *Mater. Sci. Forum* 600–603 (2009) 357–360.
- [22] M. Dudley, Y. Chen, X.R. Huang, *Mater. Sci. Forum* 600–603 (2009) 261–266.
- [23] T. Zhou, B. Raghathamachar, F. Wu, R. Dalmau, B. Moody, S. Craft, R. Schlessler, M. Dudley, Z. Sitar, *J. Electron. Mater.* 43 (2014) 838–842.
- [24] T. Zhou, B. Raghathamachar, F. Wu, M. Dudley, *MRS Symp. Proc.*, 1494 (Oxide Semiconductors and Thin Films), 261, 2014.
- [25] S. Sintonen, M. Rudzinski, S. Suihkonen, H. Jussila, M. Knetzger, E. Meissner, A. Danilewsky, T.O. Tuomi, H. Lipsanen Jr., *Appl. Phys.* 116 (2014) 083504.
- [26] P.M. Anderson, J.P. Hirth, J. Lothe, *Theory of Dislocations*, third ed., Cambridge University Press, New York, 2017.
- [27] J.D. Eshelby, A.N. Stroth, *Philos. Mag.* 42 (1951) 1401.
- [28] Y. Zhang, M. Sun, J. Perozek, Z. Liu, A. Zubair, D. Piedra, N. Chowdhury, X. Gao, K. Shepard, T. Palacios, *IEEE Electron Device Lett.* 40 (2019) 75.